Nanoscale

RSC Publishing

PAPER

View Article Online
View Journal | View Issue

Cite this: *Nanoscale*, 2013, **5**, 8105

Diffusion-controlled evolution of core–shell nanowire arrays into integrated hybrid nanotube arrays for Li-ion batteries†

Jian Jiang,[ab] Jingshan Luo,[b] Jianhui Zhu,[a] Xintang Huang,[a] Jinping Liu*[a] and Ting Yu*[b]

Received 11th April 2013
Accepted 24th May 2013

DOI: 10.1039/c3nr01786a

www.rsc.org/nanoscale

Controlled integration of multiple semiconducting oxides into each single unit of ordered nanotube arrays is highly desired in scientific research for the realization of more attractive applications. We herein report a diffusion-controlled solid–solid route to evolve simplex $Co(CO_3)_{0.5}(OH)_{0.11}H_2O$@$TiO_2$ core–shell nanowire arrays (NWs) into CoO–$CoTiO_3$ integrated hybrid nanotube arrays (NTs) with preserved morphology. During the evolution procedure, the decomposition of $Co(CO_3)_{0.5}(OH)_{0.11}H_2O$ NWs into chains of $CoCO_3$ nanoparticles initiates the diffusion process and promotes the interfacial solid–solid diffusion reaction even at a low temperature of 450 °C. The resulting CoO–$CoTiO_3$ NTs possess well-defined sealed tubular geometries and a special "inner–outer" hybrid nature, which is suitable for application in Li-ion batteries (LIBs). As a proof-of-concept demonstration of the functions of such hybrid NTs in LIBs, CoO–$CoTiO_3$ NTs are directly tested as LIB anodes, exhibiting both a high capacity (~600 mA h g^{-1} still remaining after 250 continuous cycles) and a much better cycling performance (no capacity fading within 250 total cycles) than CoO NWs. Our work presents not only a diffusion route for the formation of integrated hybrid NTs but also a new concept that can be employed as a general strategy to fabricate other oxide-based hybrid NTs for energy storage devices.

Introduction

Controlled integration of multiple semiconducting components into each single nanounit of ordered arrays of one-dimensional (1D) nanostructures is expected to allow more extraordinary functionalities and physicochemical properties that will go beyond those of arrayed nanostructures with a single configuration.[1–3] Therefore, much focus has been put on the fabrication and rational design of multi-component hybrid nanostructured arrays in recent years.[4–7] The hybridization of nanotube arrays (NTs) triggers significant interest because NTs lie at the heart of 1D nanostructures and are highly preferable for a wide spectrum of applications ranging from solar cells to Li-ion batteries (LIBs).[8–11] A general route toward the synthesis of hybrid NTs mainly involves the decoration or epitaxial growth of functional semiconducting nanomaterials onto pre-ordered NTs by means of either secondary hydrothermal processing or chemical vapor/electrochemical deposition, eventually forming a hierarchical hybrid structure.[12–15] Despite the synthetic strategy in principle providing an effective way to ensure that each nanounit in nanostructured arrays is capable of being endowed with a hybrid configuration, there are several issues associated with this strategy. Primarily, the introduced functional materials are usually attached to the outside wall of pre-ordered NTs *via* simple physical/chemical absorptions rather than a tight connection to NTs by strong chemical bonds. This is extremely detrimental to the intrinsic physicochemical properties of the as-synthesized hybrid semiconducting NTs (*e.g.*, effective electron–hole transfer from functional materials to NTs) as well as their potential applications. Additionally, the synthetic strategy inevitably makes the arrayed nanostructures reconfigure or change during the secondary hydrothermal/depositing treatment; as a result, the as-synthesized hybrid NTs tend to be heterostructured arrays with a quasi-1D or even three-dimensional (3D) architecture, no longer the pristine 1D geometric structure. This would in turn lead to the partial loss of significant 1D NT-dependent information (*e.g.*, the quantum/nanosize effect of the thin NTs wall, *etc.*)[16,17] and also complicates the analysis of their physicochemical behavior. For better understanding the unique 1D

[a]*Institute of Nanoscience and Nanotechnology, Department of Physics, Central China Normal University, Wuhan, P.R. China. E-mail: liujp@phy.ccnu.edu.cn; Fax: +86-027-67861185*

[b]*Division of Physics and Applied Physics, School of Physical and Mathematical Sciences, Nanyang Technological University, Singapore. E-mail: yuting@ntu.edu.sg*

† Electronic supplementary information (ESI) available: SEM images of $Co(CO_3)_{0.5}(OH)_{0.11}H_2O$ NWs, SEM/TEM images of CoO–$CoTiO_3$ hybrid nanotubes and the calculation of $CoTiO_3$ theoretical capacity. See DOI: 10.1039/c3nr01786a

nanostructures-derived properties, the fabrication of hybrid nanostructured arrays with preserved 1D structures is highly desired, but is still a challenge.

Diffusion-controlled approaches based on either the classical Kirkendall effect[18–22] or other non-classical diffusion effects (such as the curvature effect)[23,24] are being used in the controllable synthesis of advanced hollow materials. Particularly noteworthy is that they provide controllable ways of diffusion to fabricate high-quality oxide nanotubes.[20–22] For example, coaxial ZnO–Al_2O_3 core–shell nanowires can evolve into $ZnAl_2O_4$ nanotubes by a series of interfacial reactions involving the Kirkendall effect at a high temperature of 700 °C. However, to the best of our knowledge, nearly all of the evolved products are single-phase spinel oxide nanotubes. Yang *et al.* demonstrated the successful synthesis of Au nanocrystal-decorated Zn_2SiO_4 hybrids *via* a one-step "diffusion-facilitated" approach, which is indicative of the feasibility of this route to form smart hybrids.[25] Nevertheless, to date, there is rarely any effective preparation of all-oxide integrated hybrid nanotubes realized by the aforementioned solid-state methods.

Herein, we present an interesting and effective diffusion-controlled solid-state reaction approach to evolve the simple $Co(CO_3)_{0.5}(OH)_{0.11}H_2O$@$TiO_2$ core–shell nanowire arrays (NWs) into integrated cobalt monoxide–cobalt titanate (CoO–$CoTiO_3$) hybrid NTs. This synthetic method has several advantages as follows. First, the strategy of making hybrid NTs itself differs from previously reported approaches achieved by physical coating or chemical secondary growth. In our case, CoO diffuses into the TiO_2 layer, leading to the formation of NTs with an intriguing "inner–outer" hybrid structure with a preserved morphology. During the evolution procedure, the thermal decomposition of $Co(CO_3)_{0.5}(OH)_{0.11}H_2O$ NWs into a chain of $CoCO_3$ nanoparticles is helpful for the initiation of the diffusion process and enables the interfacial solid–solid diffusion reaction even at a low temperature of 450 °C. Second, the evolved products possess a well-defined NT architecture offering both oriented pathways for electron transfer and interior hollow cavities for ion transport, which is recognised as a suitable and preferred structure for Li storage.[8] All nanotubes are well separated and arrayed on the current collector, and are capable of serving as the anode directly, without adding any polymer binders or conducting agents. Also, the prepared NTs have a hybrid composition, generating synergistic benefits induced by the combination of distinct functional components when used as anodes of LIBs. The outer titanate layer with less capacity storage and volume change may function not only as a good buffer material to alleviate unfavorable volume expansion of CoO, but also a robust "backbone" to preserve NTs against the structure pulverization caused by repeated Li insertion–extraction.[26,27] As a proof-of-concept demonstration of its Li-storage ability, the CoO–$CoTiO_3$ hybrid NTs electrode is capable of delivering both high capacity (~600 mA h g^{-1} after 250 continuous cycles) and showing much superior cycling performance (no capacity fading within 250 total cycles) to single-phased CoO NWs when tested as a binder-free electrode for LIBs.

Experimental

Synthesis of CoO–$CoTiO_3$ hybrid NTs on Ti foil

All reagents below were received from Sigma-Aldrich Co. (USA) and used without further purification. $Co(CO_3)_{0.5}(OH)_{0.11}H_2O$ NWs were employed as the precursor materials and prepared using a facile hydrothermal method according to the previous literature.[28] A piece of clean Ti foil ($30 \times 10 \times 0.2$ mm^3) was immersed into a Teflon-lined stainless steel autoclave in which there was a 50 mL homogeneous solution containing 0.582 g $Co(NO_3)_2 \cdot 6H_2O$ and 0.6 g $CO(NH_2)_2$. The autoclave was sealed and kept still in an electric oven at a temperature of 95 °C for 8 h. When the equipment had cooled down to room temperature, the sample was taken out, washed with distilled water several times and dried in an electric oven. After that, a TiO_2 layer with a thickness of 10 nm was conformably deposited onto the $Co(CO_3)_{0.5}(OH)_{0.11}H_2O$ NWs by the atomic layer deposition (ALD) technique (Beneq TFS-200, Finland) at 120 °C, with titanium tetrachloride (99.99%, Sigma Aldrich) and H_2O as the Ti and O precursors, respectively. The as-formed intermediate was then heated to 450 °C at a heating rate of ~10 °C min^{-1} under a constant Ar flow of 80 sccm and held for 1 h, allowing for the complete transformation of $Co(CO_3)_{0.5}(OH)_{0.11}H_2O$@$TiO_2$ NWs into CoO–$CoTiO_3$ hybrid NTs. After cooling down to room temperature naturally, the sample was removed and dried at 60 °C in an electric oven.

Sample characterization

The morphology and the crystal structure of the as-made products were characterized with a JEOL JSM-6700F field emission scanning electron microscope (FE-SEM) with energy dispersive X-ray spectroscopy (EDS), and a JEM 2010F high-resolution transmission electron microscope (HR-TEM). Raman spectroscopy (Witech. CRM200, 532 nm) was also used to characterize the products. X-ray powder diffraction (XRD) patterns were recorded on a Bruker D8 Advance diffractometer using Cu Kα radiation ($\lambda = 1.5418$ Å). The mass of the electrode materials was measured on a microbalance with an accuracy of 0.01 mg (A&D Company N92, Japan).

Electrochemical measurements

Electrochemical measurements were performed using two-electrode CR2032 (3 V) coin-type cells with Li foil as both counter and reference electrodes at ambient temperature. Herein, Ti foil was chosen to be the current collector since it does not alloy with metallic Li. The sample was cut into a disk with a surface area of ~1 cm^2 and directly used as the working electrode. The electrolyte solution was 1 M $LiPF_6$ dissolved in a mixture of ethylene carbonate (EC) and diethyl carbonate (DEC) (1 : 1 by volume). Cell assembly was performed in an argon-filled glovebox (Mbraun, Unilab, Germany) with both moisture and oxygen contents below 1.0 ppm. Galvanostatic charge–discharge tests were performed using a NEWARE battery tester in a voltage window of 0.005–3 V. Before battery testing, the cells were aged for 10 h.

Results and discussion

The overall evolution process of the CoO–$CoTiO_3$ hybrid NTs is shown in Scheme 1. The $Co(CO_3)_{0.5}(OH)_{0.11}H_2O$ NW precursors grown on a Ti substrate were pre-synthesized *via* a hydrothermal method following our previous work.[28] For step I, the prepared single-crystalline $Co(CO_3)_{0.5}(OH)_{0.11}H_2O$ NWs (Fig. S1†) are conformably coated with a 10 nm-thick layer of TiO_2 by means of atomic layer deposition (ALD), which is a thin-film deposition technique based on self-limiting surface reactions.[29–31] This technique is preferable for the deposition of a TiO_2 thin film onto ordered NWs as it offers precise thickness control and ensures the uniform coating of each nanowire. The next step is the calcination of $Co(CO_3)_{0.5}(OH)_{0.11}H_2O$@$TiO_2$ NWs in an Ar atmosphere. After a heating treatment conducted at 450 °C for 1 h, the simplex core–shell NWs successfully evolve into high-quality CoO–$CoTiO_3$ hybrid NTs.

The crystal structure and phase purity of CoO–$CoTiO_3$ hybrid NTs were examined by X-ray diffraction (XRD), as shown in Fig. 1(a). For comparison, the XRD pattern of pure CoO is also provided. Evidently, except for the appearance of diffraction peaks originating from either the CoO or Ti substrate, two novel diffraction peaks are located at 2θ of 32.8° and 35.4°, which are highly consistent with $CoTiO_3$ (JCPDS card no. 15-0866) and correspond to its (104) and (110) facets, respectively. The result of decomposition of the cobalt carbonate precursors is highly consistent with results of our previous work.[6,28] $Co(CO_3)_{0.5}(OH)_{0.11}H_2O$ merely decomposes to CoO;[28] no peaks from impurities such as Co_3O_4 are detected. Energy dispersive X-ray spectroscopy (EDS) and Raman spectroscopy are used to characterize the aligned CoO–$CoTiO_3$ hybrid NTs. Fig. 1(b) illustrates that the as-synthesized NTs contain Co, Ti, and O (Co–Ti atomic ratio obtained from EDS is 85.87 : 14.13, equivalent to 6 : 1), suggesting that no foreign elements are involved in the evolution process. The Raman spectrum (Fig. 1(c)) shows that there are five distinguishable Raman bands derived from the hybrid sample; all bands located at 235, 266, 336, 382, and 695 cm^{-1} are in good agreement with the characteristic bands or the second-order scattering of $CoTiO_3$.[32–34] The samples were also examined by scanning electron microscopy (SEM) and transmission electron microscopy (TEM). Fig. 2(a) shows that the hybrid products perfectly inherit the geometric morphology of the precursor NWs. Plenty of 1D nanostructures are clearly separated and uniformly arrayed on the Ti metal substrate, quite similar to the case of previously reported CoO NWs made by thermal treatment of $Co(CO_3)_{0.5}(OH)_{0.11}H_2O$ NWs.[28] TEM examination reveals that they have a sealed tubular structure with a smooth surface, which is ivery distinct from the porous CoO NWs obtained by annealing the $Co(CO_3)_{0.5}(OH)_{0.11}H_2O$ precursors under exactly the same conditions. The mean diameter of the NTs is around 150 nm and they have a thin tubular wall of ~15 nm, indicating that the hybrid NTs wall is quite permeable to Li ions. To gain insight into the inner structure of such CoO–$CoTiO_3$ hybrid NTs, the high-resolution TEM (HRTEM) examination was performed at different parts of one nanotube surface (schematically indicated in insets of Fig. 2(e) and (f), and also see the TEM image in Fig. S2†). The lattice fringes (white) with spacings of 0.465 and 0.254 nm in Fig. 2(e) successively correspond to the (003) and (110) planes of $CoTiO_3$. The inset fast Fourier transform (FFT) pattern also confirms the former HRTEM result and further reveals that the hybrid NTs surface is well crystallized (no longer in an amorphous state).[35] However, two sets of lattices are found in the cross-sectional observation (Fig. 2(f)). The lattices (yellow) with distances of 0.246 nm and 0.213 nm at the inner side of the nanotubes are successively attributed to the (111) and (200) facets of cubic CoO, while lattices present at the outside region of the tube wall are all indexed to the (003) facet of $CoTiO_3$. This fully confirms the as-formed NTs have a unique integrated "CoO (inner)–$CoTiO_3$ (outer)" hybrid configuration.

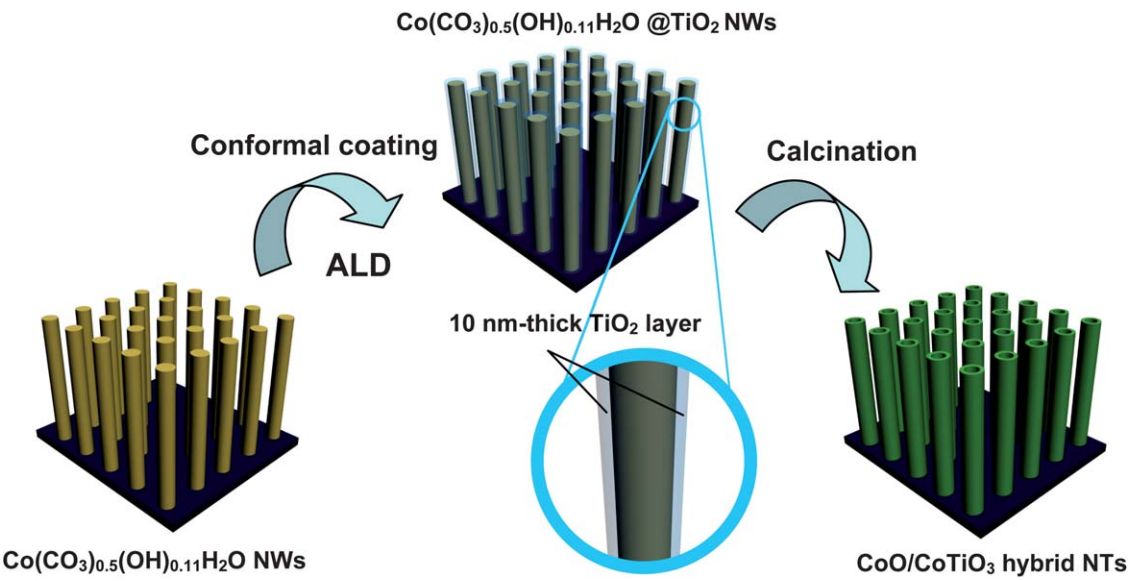

Scheme 1 Schematic illustration of the evolution process of CoO–$CoTiO_3$ hybrid NTs on a Ti substrate.

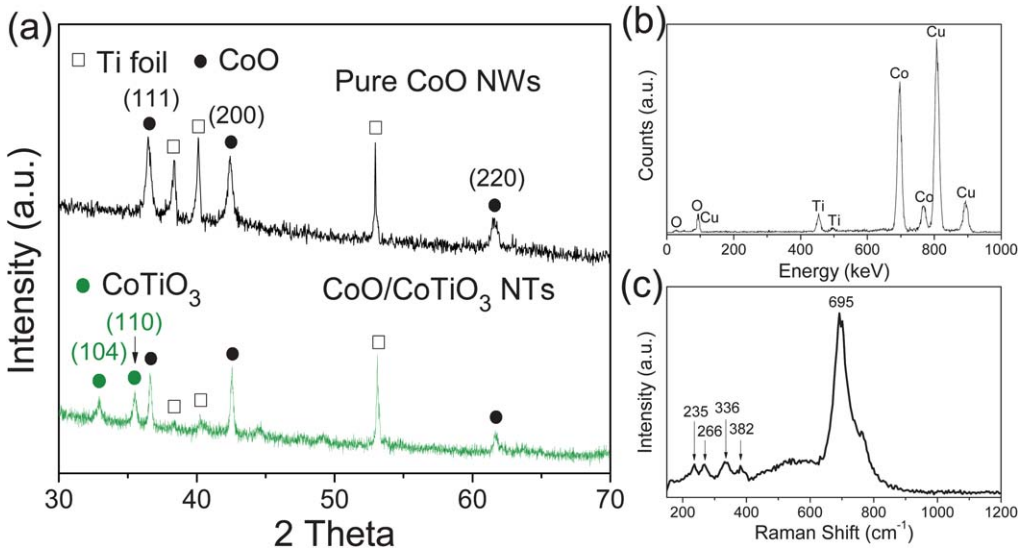

Fig. 1 (a) XRD pattern, (b) EDS spectrum and (c) Raman spectrum of the CoO–$CoTiO_3$ hybrid NTs grown on a Ti substrate. For comparison, the XRD pattern of pure CoO NWs is also provided and shown in (a).

What needs to be unveiled is how such hybrid NTs evolve during calcination treatment. To make this point clear and try to explore the evolution mechanism, we purposely used TEM observations (Fig. 3) and XRD measurements (Fig. 4) to monitor the entire evolution process. Representative TEM images of $Co(CO_3)_{0.5}(OH)_{0.11}H_2O$@$TiO_2$ NWs are displayed in Fig. 3(a) and (b). Prior to heating, the morphology of the $Co(CO_3)_{0.5}(OH)_{0.11}H_2O$@$TiO_2$ NW intermediate is nearly the same with that of the NW precursor except that there exists a uniform TiO_2 layer (~10 nm) on the $Co(CO_3)_{0.5}(OH)_{0.11}H_2O$ nanowires (Fig. 3(b)). Diffraction peaks appearing at 2θ of 17.5°, 35.4° and 44.6° in the XRD pattern (Fig. 4, red) are in good agreement with those of orthorhombic cobalt carbonate hydroxide hydrate (JCPDS card no. 48-0083), corresponding to its (020), (320) and (022) facets, respectively. Signals from the deposited TiO_2 layer are not detected because of both the low weight ratio (less than 13%, calculated from former EDS data) and the amorphous nature of TiO_2 generated from the hydrolysis of titanium tetrachloride at a low temperature.[31] Fig. 3(c) and (d) show TEM images of samples when the heating temperature rises to 200 °C. As noted, the inner solid nanowires start to become porous but the morphology of the outer TiO_2 layer remains unchanged. The XRD pattern (Fig. 4, blue) shows the presence of a sharp diffraction peak at a 2θ of 62.1°, corresponding to the (122) facet of $CoCO_3$ (JCPDS card no. 11-0692). This reflects that at this evolution stage, the inner $Co(CO_3)_{0.5}(OH)_{0.11}H_2O$ NWs are subject to a thermal decomposition and afterwards change into porous $CoCO_3$ NWs. Simultaneously, the crystallinity of the TiO_2 layer becomes pronounced as evidenced by the presence of diffraction peaks, especially the (400), ($\bar{3}$11), ($\bar{4}$02) peaks from monoclinic TiO_2 (JCPDS card no. 46-1237). Upon raising the heating temperature to 300 °C under constant Ar flow, the $CoCO_3$ NW core becomes more porous, and resembles a chain of connected nanoparticles (Fig. 3(e) and (f)). The further decomposition of the carbonate core should be the reason to form this porous structure, as suggested by the decreased intensity of the (122) peak of $CoCO_3$ from the XRD pattern (Fig. 4, black). In addition, it is noteworthy that all diffraction peaks belonging to TiO_2 are completely missing, which might be ascribed to the occurrence of solid-state diffusion reactions. Fig. 3(g) and (h) display TEM observations of samples when heated to 450 °C. As observed, the porous NW core disappears completely, suggesting the successful generation of CoO–$CoTiO_3$ hybrid NTs. The XRD pattern (Fig. 4, green) shows that two distinct functional components, CoO and $CoTiO_3$, are cleverly integrated after the overall evolution process. The hybrid NTs formation can be ascribed to the process of the generated CoO diffusing into the TiO_2 layer *via* a non-classical curvature effect,[23,24] and in the meantime, part of the CoO reacts with TiO_2 in a solid–solid way, resulting in the generation of a hollow tubular structure. The involved chemical reactions can be generally expressed as follows:

$$Co(OH)_x(CO_3)_{0.5(2-x)}\cdot nH_2O \rightarrow Co(CO_3)_{0.5(2-x)} + (n + x/2)H_2O$$

$$Co(CO_3)_{0.5(2-x)} \rightarrow CoO + 0.5(2 - x)CO_2$$

$$CoO\ (partial) + TiO_2 \rightarrow CoTiO_3$$

The electrochemical performance of the evolved CoO–$CoTiO_3$ NTs was evaluated in a two-electrode system using Li metal as the counter electrode. The hybrid NTs product is directly used as the anode electrode without adding any conductive agents or polymer binders. Fig. 5(a) shows the voltage–capacity profiles of CoO–$CoTiO_3$ hybrid NTs in the potential window of 50–3000 mV *vs.* Li^+/Li at a current density of ~0.3 A g^{-1} for the 1st, 2nd, 10th, 50th, 100th and 150th cycles, respectively. At the 1st cycle, the hybrid NTs electrode exhibits charge/discharge capacities of ~395.2 and ~645.5 mA h g^{-1},

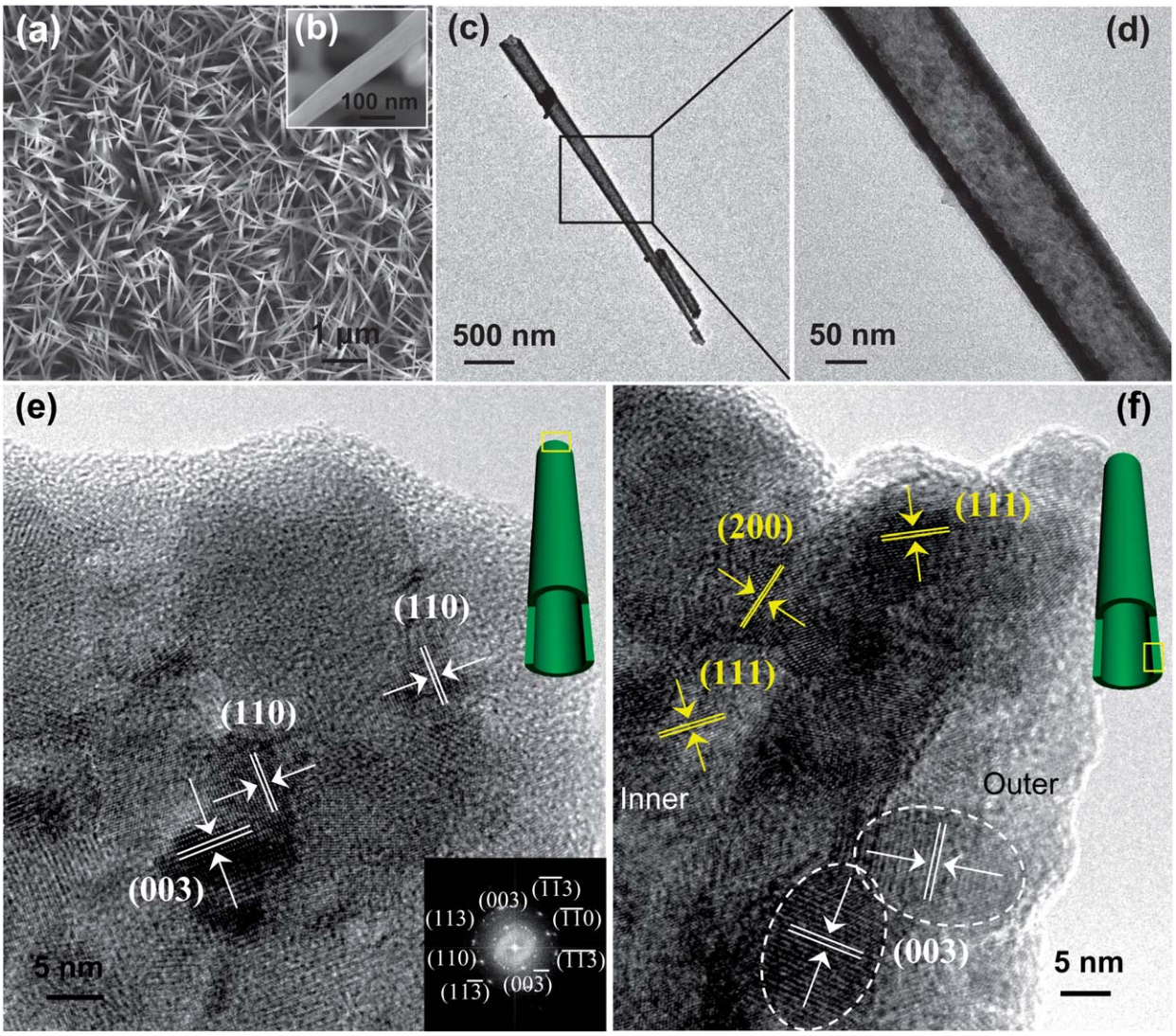

Fig. 2 (a and b) SEM and (c and d) TEM images of CoO–$CoTiO_3$ hybrid NTs. (e) HRTEM observations of the CoO–$CoTiO_3$ hybrid NTs on the nanotube surface and (f) the cross-section profile of the tube wall. The inset in (e) is the FFT pattern of the hybrid nanotube surface.

respectively, and an initial coulombic efficiency of ~61.2%. The capacity loss in the initial cycle is mainly ascribed to irreversible processes involving the decomposition of the electrolyte, inevitable formation of a solid electrolyte interface (SEI) and trapping of some Li in lattices, which are common for anode materials, especially with confined hollow nanostructures.[36–38] In the subsequent ten cycles, the electrode has stable charge/discharge capacities with an average value of ~370 mA h g^{-1} (comparable to the capacity value 372 mA h g^{-1} of commercial graphite) and high coulombic efficiencies increased up to ~99%, indicative of good reversibility toward lithiation–delithiation. Over ten cycles, it is interesting to note that both charge and discharge capacities increase progressively; the discharge capacities in the 50th and 100th cycle are around 450 and 540 mA h g^{-1}, respectively, both higher than the initial values. Strikingly, even at the 150th cycle, the CoO–$CoTiO_3$ hybrid NTs electrode is able to deliver a discharge capacity of as high as ~585 mA h g^{-1}, which is an increase to ~162% relative to the capacity value in the 10th cycle.

In order to understand the "capacity increase" phenomenon and explore detailed electrochemical processes between lithium and the hybrid NTs, the differential capacity plots (dQ/dV) of the 1st, 2nd, 50th and 150th cycle are successively presented in Fig. 5(b)–(e). Fig. 5(b) depicts that there are two reduction peaks appearing in the 1st cathodic process, corresponding to different types of lithiation reactions. The one broad peak centered at 1105 mV is assigned to a reduction process by following a unique conversion mechanism,[39] wherein Co^{II} in hybrid NTs is transformed into Co^0 nano-domains uniformly dispersed in a Li_2O matrix.[40] The other sharp peak is located at 580 mV in the 1st discharge but its disappearance in the subsequent cycles is related to the formation of a polymer/gel-like film on the CoO–$CoTiO_3$ hybrid NTs. For initial anodic polarization, only one peak is found at the potential of ~1995 mV, which is attributed to the complex phase transformations of Co^0 back to Co^{II} and agrees well with the results of previous work.[28,41] The differential capacity plot of the 2nd cycle (Fig. 5(c)) is distinct from the initial case. Except for the reduction peak

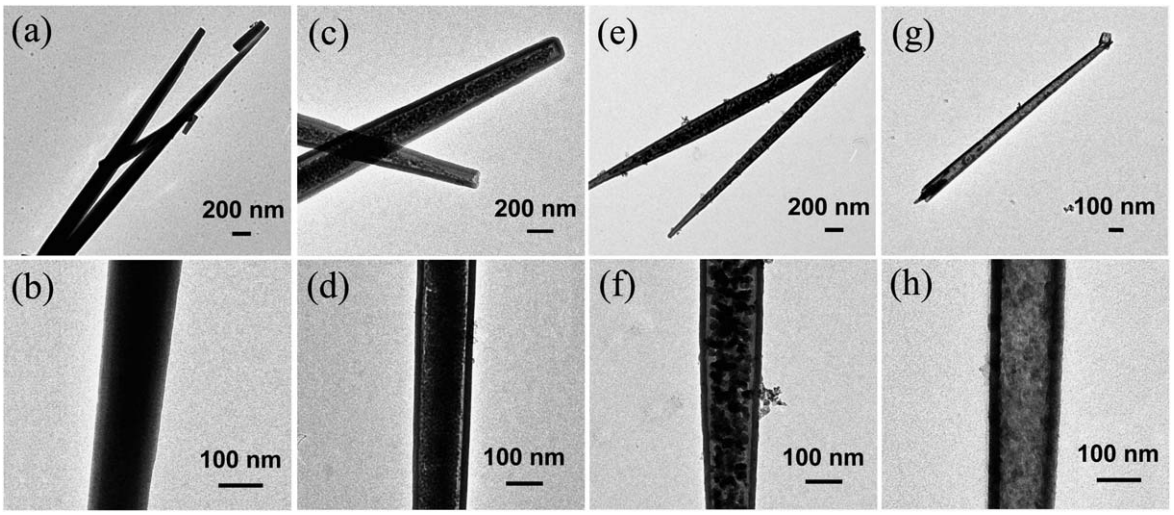

Fig. 3 TEM observations of samples obtained at the evolution stages when the heating temperature reaches (a and b) room temperature, (c and d) 200 °C, (e and f) 300 °C, (g and h) 450 °C, respectively.

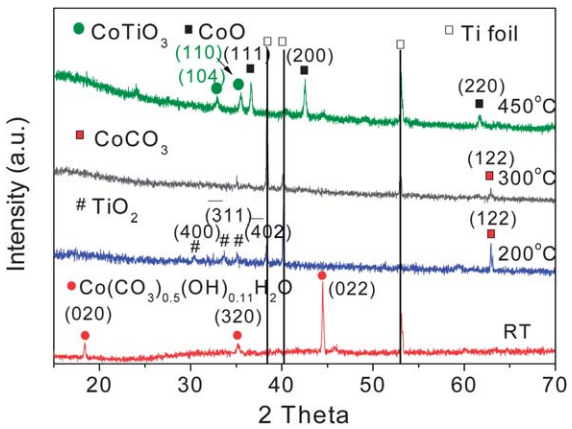

Fig. 4 XRD patterns of samples obtained at different evolution stages.

aforementioned in the broad range of 700–1200 mV, two additional peaks are present during the 2nd cathodic process, a dominating one at 1365 mV and a weak one at 1640 mV. According to the literature, both novel peaks are associated with Li intercalation reactions, especially for nanostructured titanium oxide species.[42,43] The presence of certain cathodic peaks reveals that Ti^{IV} participates in lithiation reactions and makes contributions to the capacity of lithium storage. The anodic peak for the 2nd cycle is identical to that of the initial one except for a slight potential shift (53 mV) in the positive direction. Fig. 5(d) and (e) successively display the differential capacity plots at the 50th and 150th cycle. With an increasing number of cycles, the cathodic peak either at 1025 mV (for 50th cycle) or 1075 mV (for 150th cycle) becomes distinct, and its intensity is somewhat larger than that of the 2nd cycle. This implies that more Co^{II} has been "activated" and participates in redox

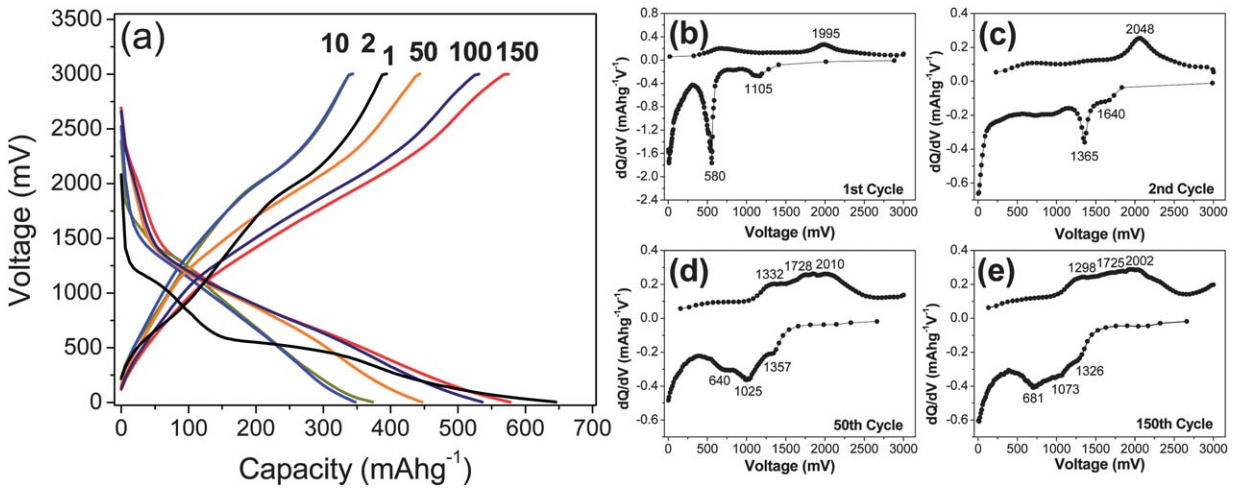

Fig. 5 (a) Galvanostatic charge–discharge profiles of CoO–$CoTiO_3$ hybrid NTs in a potential window of 50–3000 mV *vs.* Li^+/Li at a current density of ~0.3 A g^{-1} for 150 cycles and (b–e) corresponding differential capacity plots (d*Q*/d*V*) for the 1st, 2nd, 50th and 150th cycle.

reactions with Li, eventually leading to the gradual enhancement of charge–discharge capacities. Moreover, a new and particular reduction peak emerges at a potential of 640–681 mV, far lower than the reduction potentials of either TiO_2 or CoO, but very close to the peak potential of ~580 mV (only appearing during initial discharge). This may be related to the additional generation of a SEI film inside the central cavity of the nanotubes or on their damaged areas, such as pores and edges formed through repeated Li insertion–desertion.[44] It is worth noting that a novel anodic peak appears at a potential of 1298–1332 mV after 50 cycles. Given the outstanding catalytic properties of nanosized transition metals (*e.g.*, Fe, Ni, Co, Mn) and by referring to related reports,[9,45–48] we believe that the yielded Co^0 nano-domains may act as catalysts for the decomposition of the SEI film when the LIBs are cycled. The remaining broad anodic peak at 1725–1728 mV derives from the reversible Li deintercalation reaction for Ti^{IV}.[43a] Besides, with the increase of cycle numbers, the values of anodic peaks are shifted. The decrease of the anodic potential (*e.g.*, from 2048 mV in the 2nd cycle to 2002 mV in the 150th cycle) reveals that the CoO–$CoTiO_3$ hybrid electrode has better electrochemical kinetics due to the reduced over-potential η upon cycling ($\eta = E_{meas} - E_{eq}$, where E_{eq} is the equilibrium potential and E_{meas} is the experimentally measured potential).[43b] This might be caused by the activation of the NTs' structure and thus the decrease in polarization.

We now discuss how stable the capacity upon repeated cycling is. Fig. 6(a) shows the cycling performance of CoO–$CoTiO_3$ hybrid NTs at a constant current rate of 0.3 A g^{-1}. For comparison, the cycling test of pure CoO NWs is also conducted under the same electrochemical conditions (inset of Fig. 6(a)). Evidently, the hybrid CoO–$CoTiO_3$ NTs exhibit far better cycling behavior than single-component CoO NWs in terms of long-term cyclic stability, coulombic efficiency and capacity retention. The CoO–$CoTiO_3$ hybrid NTs electrode can deliver a high reversible capacity of 585 mA h g^{-1} (equivalent to 154% of the capacity in the initial reversible discharge) after going through 150 cycles. While for the bare CoO NW electrode, only a poor capacity of ~392 mA h g^{-1} can be retained after 50 cycles (~49% reversible capacity retention). It is also noted that the charge–discharge capacity of the CoO–$CoTiO_3$ NTs is gradually increased and is maintained at ~580 mA h g^{-1} over 130 cycles, which is contrary to the continuous capacity degradation of the CoO NWs electrode. The cycling performance of the CoO–$CoTiO_3$ hybrid NTs at programmed current densities was tested after the galvanostatic charge–discharge cycles (Fig. 6(b)). As can be seen, the hybrid electrode still exhibits a stable cyclic behavior at each current density (~100% coulombic efficiency). The electrode is initially subjected to continuous cycling 10 times at 0.3 A g^{-1}, during which it delivers a mean capacity of ~585 mA h g^{-1} without noticeable decay. When cycled at a large current density of 4.00 A g^{-1}, the electrode still retains a capacity of up to ~237 mA h g^{-1}, which is still comparative to that of bare porous CoO NWs (~210 mA h g^{-1} at ~4.00 A g^{-1}).[28] Upon successively switching the current densities after 62 cycles, the capacity is able to recover. These results highlight both the good capacity retention and rate capability of CoO–$CoTiO_3$ hybrid NTs. As is known, the maintenance of the NTs electrode architecture is a prerequisite to realize LIBs with both good long-cycling and fast charge–discharge properties.[49] To test this, SEM and TEM observations were performed on the electrode after 150 times of charge–discharge cycles. It is shown that a large number of sphere-like structures appear on top of the cycled electrode (Fig. S3a†), which is caused by the volume expansion and aggregation of nanotube tips, as well as the SEI film formation. It is also noted that the surface of the NTs becomes porous compared to the initially smooth surface (see Fig. S3c and d and S4a–c†), as a result of repeated Li insertion–desertion processes. Nonetheless, the electrode still preserves both the arrayed configurations and a good contact to the current collector even after 150 cycles, without any severe cracks or pulverization. Besides, we proposed that the yielded porous structure also increases the active surface areas in contact with the electrolyte, and thus might be beneficial to the good rate behavior of CoO–$CoTiO_3$ hybrid NTs.

The following aspects may be responsible for the enhanced cyclic stability of this electrode when compared to bare CoO NWs. On the one hand, the NT architecture itself is preferable

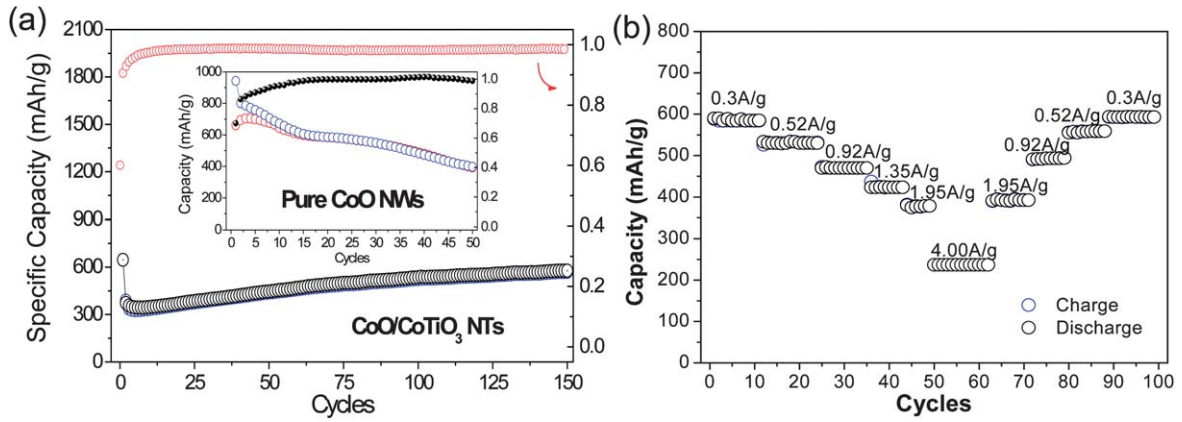

Fig. 6 (a) Cycling performance of CoO–$CoTiO_3$ hybrid NTs at a constant current rate of 0.3 A g^{-1}. (b) Cycling responses (after 150 charge–discharge cycles) of CoO–$CoTiO_3$ hybrid NTs at programmed current densities.

for electrochemical applications, particularly for fast charge–discharge LIBs since the oriented 1D arrayed hollow structure offers both quick electron-transfer pathways and ion-transport cavities. Moreover, the interior void space in NTs can also help to accommodate structural deformations. On the other hand, in the hybrid NT system, the inner CoO core inside the NTs makes a dominating contribution to the overall capacity due to its high theoretical capacity of ~716 mA h g^{-1}. While for the titanate skin layer with a lower theoretical capacity (see calculation details in the ESI†), it is capable of acting like an "armor", which may not only restrict the volume expansion of inner CoO but also protect the architecture of overall NTs from collapse or even pulverization. This leads to their better cycling stability as well as long cycling endurance.

Conclusions

In summary, an interesting diffusion-controlled solid–solid approach has been presented to fabricate CoO–$CoTiO_3$ hybrid NTs using core–shell $Co(CO_3)_{0.5}(OH)_{0.11}H_2O$@$TiO_2$ NWs as the starting material without reconfiguring the 1D nanostructures. During the evolution process, $Co(CO_3)_{0.5}(OH)_{0.11}H_2O$ NWs first decompose into $CoCO_3$ nanoparticles, which promotes the interfacial CoO–TiO_2 diffusion reaction even at a low temperature of 450 °C. These formed CoO–$CoTiO_3$ NTs have well-defined sealed tubular geometries and a special "inner–outer" hybrid nature, and is regarded as an excellent anode material for LIBs. As a proof-of-concept demonstration of the functions of such hybrid NTs in LIBs, the CoO–$CoTiO_3$ NTs electrode can exhibit both high capacity (~600 mA h g^{-1} retained after continuous 250 testing cycles) and much better cycling performance (no capacity fading over 250 total cycles) than CoO NWs. These good battery performances may be attributed to the well-designed NT architecture, the inner–outer hybrid configuration yielding some synergistic effects, and porous features of the outer $CoTiO_3$ along with increased cycles. Moreover, our developed concept can be employed as a general strategy for future fabrication of other promising oxide-based hybrid NTs by using carbonate as the starting material.

Acknowledgements

Liu Jinping and Xintang Huang thank the National Natural Science Foundation of China (no. 51172085, 51102105, 11104088), the Key Project of Natural Science Foundation of Hubei Province (No. 2011CDA092) and Self-determined Research Funds of CCNU from the Colleges' Basic Research and Operation of MOE (CCNU12A01009). Yu Ting is thankful for the support of the Singapore National Research Foundation under NRF RF Award no. NRFRF2010-07. Authors thank Prof. Fan Hongjin at Nanyang Technological University for the ALD coating.

Notes and references

1 J. Jiang, Y. Y. Li, J. P. Liu, X. T. Huang, C. Z. Yuan and X. W. Lou, *Adv. Mater.*, 2012, **24**, 5166.
2 J. P. Liu, J. Jiang, C. W. Cheng, H. X. Li, J. X. Zhang, H. Gong and H. J. Fan, *Adv. Mater.*, 2011, **23**, 2076.
3 L. Q. Mai, X. Xu, C. H. Han, Y. Z. Luo, L. Xu, Y. M. Wu and Y. L. Zhao, *Nano Lett.*, 2011, **11**, 4992.
4 B. Liu, J. Zhang, X. F. Wang, G. Chen, D. Chen, C. Zhou and G. Z. Shen, *Nano Lett.*, 2012, **12**, 3005.
5 J. H. Kim, K. Zhu, Y. F. Yan, C. L. Perkins and A. J. Frank, *Nano Lett.*, 2010, **10**, 4099.
6 C. Guan, J. P. Liu, C. W. Cheng, H. X. Li, X. L. Li, W. Zhou, H. Zhang and H. J. Fan, *Energy Environ. Sci.*, 2011, **4**, 4496.
7 J. P. Liu, J. Jiang, M. Bosman and H. J. Fan, *J. Mater. Chem.*, 2012, **22**, 2419.
8 J. Liu, G. Z. Cao, Z. G. Yang, D. H. Wang, D. Dubois, X. D. Zhou, G. L. Graff, L. R. Pederson and J. G. Zhang, *ChemSusChem*, 2008, **1**, 676.
9 J. Jiang, Y. Y. Li, J. P. Liu and X. T. Huang, *Nanoscale*, 2011, **3**, 45.
10 J. P. Liu, Y. Y. Li, H. J. Fan, Z. H. Zhu, J. Jiang, R. M. Ding, Y. Y. Hu and X. T. Huang, *Chem. Mater.*, 2010, **22**, 212.
11 J. Z. Wang, N. Du, H. Zhang, J. X. Yu and D. R. Yang, *J. Phys. Chem. C*, 2011, **115**, 11302.
12 D. A. Wang, Y. Liu, C. W. Wang, F. Zhou and W. M. Liu, *ACS Nano*, 2009, **3**, 1249.
13 F. X. Xiao, *J. Phys. Chem. C*, 2012, **116**, 16487.
14 S. H. Kang, J. Y. Kim, Y. Kim, H. S. Kim and Y. E. Sung, *J. Phys. Chem. C*, 2007, **111**, 9614.
15 L. Y. Fan and S. H. Yu, *Phys. Chem. Chem. Phys.*, 2009, **11**, 3710.
16 M. S. Sander, M. J. Cote, W. Gu, B. M. Kile and C. P. Tripp, *Adv. Mater.*, 2004, **16**, 2052.
17 T. J. Park, A. A. Levchenko, H. J. Zhou, S. S. Wong and A. Navrotsky, *J. Mater. Chem.*, 2010, **20**, 8639.
18 H. J. Fan, U. Gösele and M. Zacharias, *Small*, 2007, **3**, 1660.
19 Y. Yang, D. S. Kim, R. Scholz, M. Knez, S. M. Lee, U. Gösele and M. Zacharias, *Chem. Mater.*, 2008, **20**, 3487.
20 H. J. Fan, M. Knez, R. Scholz, K. Nielsch, E. Pippel, D. Hesse, M. Zacharias and U. Gosele, *Nat. Mater.*, 2006, **5**, 627.
21 H. J. Fan, M. Knez, R. Scholz, D. Hesse, K. Nielsch, M. Zacharias and U. Gösele, *Nano Lett.*, 2007, **7**, 993.
22 R. M. Ding, J. P. Liu, J. Jiang, Y. Y. Li, Y. Y. Hu, X. X. Ji, Q. B. Chi, F. Wu and X. T. Huang, *Chem. Commun.*, 2009, 4548.
23 R. Mukherjee, T. Chakrabarti, E. A. Anumol, T. A. Abinandanan and N. Ravishankar, *ACS Nano*, 2011, **5**, 2700.
24 E. A. Anumol, B. Viswanath, P. G. Ganesan, Y. F. Shi, G. Ramanath and N. Ravishankar, *Nanoscale*, 2010, **2**, 1423.
25 Y. Yang, R. B. Yang, H. J. Fan, R. Scholz, Z. P. Huang, A. Berger, Y. Qin, M. Knez and U. Gösele, *Angew. Chem., Int. Ed.*, 2010, **49**, 1442.
26 X. W. Lou, D. Deng, J. Y. Lee, J. Feng and L. A. Archer, *Adv. Mater.*, 2008, **20**, 258.
27 X. W. Lou, Y. Wang, C. Yuan, J. Y. Lee and L. A. Archer, *Adv. Mater.*, 2006, **18**, 2325.
28 J. Jiang, J. P. Liu, R. M. Ding, X. X. Ji, Y. Y. Hu, X. Li, A. Z. Hu, F. Wu, Z. H. Zhu and X. T. Huang, *J. Phys. Chem. C*, 2010, **114**, 929.
29 D. W. Liu, Y. Y. Liu, S. L. Candelaria and G. Z. Cao, *J. Vac. Sci. Technol., A*, 2012, **30**, 01A123.

30 Y. S. Jung, A. S. Cavanagh, L. A. Riley, S. H. Kang, A. C. Dillon, M. D. Groner, S. M. George and S. H. Lee, *Adv. Mater.*, 2010, **22**, 2172.
31 M. N. Liu, X. L. Li, S. K. Karuturi, A. I. Y. Tok and H. J. Fan, *Nanoscale*, 2012, **4**, 1522.
32 B. Jongsomjit, C. Sakdamnuson, J. G. Goodwin and P. Praserthdam, *Catal. Lett.*, 2004, **94**, 209.
33 Y. Brik, M. Kacimi, M. Ziyad and F. Bozon-Verdurazy, *J. Catal.*, 2001, **202**, 118.
34 U. Balachandran and N. G. Eror, *J. Solid State Chem.*, 1982, **42**, 276.
35 Y. N. Zhu, W. Chen, C. Y. Nan, Q. Peng, R. J. Wang and Y. D. Li, *Cryst. Growth Des.*, 2011, **11**, 4406.
36 B. Wang, J. S. Chen, H. B. Wu, Z. Y. Wang and X. W. Lou, *J. Am. Chem. Soc.*, 2011, **133**, 17146.
37 X. W. Lou, D. Deng, J. Y. Lee and L. A. Archer, *Chem. Mater.*, 2008, **20**, 6562.
38 W. M. Zhang, J. S. Hu, Y. G. Guo, S. F. Zheng, L. S. Zhong, W. G. Song and L. J. Wan, *Adv. Mater.*, 2008, **20**, 1160.
39 P. Poizot, S. Laruelle, S. Grugen, L. Dupont and J. M. Tarascon, *Nature*, 2000, **407**, 496.
40 Y. G. Li, B. Tan and Y. Y. Wu, *Nano Lett.*, 2008, **8**, 265.
41 J. Jiang, J. H. Zhu, R. M. Ding, Y. Y. Li, F. Wu, J. P. Liu and X. T. Huang, *J. Mater. Chem.*, 2011, **21**, 15969.
42 D. Barreca, G. Carraro, A. Gasparotto, C. Maccato, M. Cruz-Yusta, J. L. Gómez-Camer, J. Morales, C. Sada and L. Sánchez, *ACS Appl. Mater. Interfaces*, 2012, **4**, 3610.
43 (*a*) G. F. Ortiz, I. Hanzu, P. Lavela, P. Knauth, J. L. Tirado and T. Djenizian, *Chem. Mater.*, 2010, **22**, 1926; (*b*) P.-L. Taberna, S. Mitra, P. Poizot, P. Simon and J.-M. Tarascon, *Nat. Mater.*, 2006, **5**, 567.
44 C. Masarapu, V. Subramanian, H. W. Zhu and B. Q. Wei, *Adv. Funct. Mater.*, 2009, **19**, 1008.
45 C. Q. Zhang, J. P. Tu, Y. F. Yuan, X. H. Huang, X. T. Chen and F. Mao, *J. Electrochem. Soc.*, 2007, **154**, A65.
46 W. M. Zhang, X. L. Wu, J. S. Hu, Y. G. Guo and L. J. Wan, *Adv. Funct. Mater.*, 2008, **18**, 3941.
47 J. S. Chen, C. M. Li, W. W. Zhou, Q. Y. Yan, L. A. Archer and X. W. Lou, *Nanoscale*, 2009, **1**, 280.
48 W. Zhou, C. Cheng, J. Liu, Y. Y. Tay, J. Jiang, X. Jia, J. Zhang, H. Gong, H. H. Hng, T. Yu and H. J. Fan, *Adv. Funct. Mater.*, 2011, **21**, 2439.
49 J. P. Liu, Y. Y. Li, R. M. Ding, J. Jiang, Y. Y. Hu, X. X. Ji, Q. B. Chi, Z. H. Zhu and X. T. Huang, *J. Phys. Chem. C*, 2009, **113**, 5336.